

# PdAg Alloy Nanocatalysts: Toward Economically Viable Nitrite Reduction in Drinking Water

Jacob P. Troutman, Hao Li, Alison M. Haddix, Benjamin A. Kienzle, Graeme Henkelman,\*  
Simon M. Humphrey,\* and Charles J. Werth\*



Cite This: *ACS Catal.* 2020, 10, 7979–7989



Read Online

ACCESS |



Metrics & More



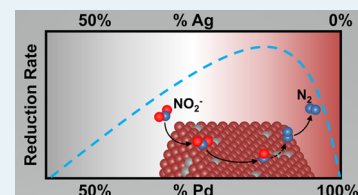
Article Recommendations



Supporting Information

**ABSTRACT:** Nitrite ( $\text{NO}_2^-$ ) is the primary reduction product of nitrate ( $\text{NO}_3^-$ ), which is the most predominant contaminant in global freshwater. Both species present major environmental challenges;  $\text{NO}_2^-$  is also highly toxic to humans. Available technologies for the removal of  $\text{NO}_3^-$  and  $\text{NO}_2^-$  from potable water are hampered by a number of issues, which limit their widespread usage. Catalytic degradation of  $\text{NO}_3^-$  and  $\text{NO}_2^-$  is a potentially disruptive technology. However, the high cost of palladium metal required for this process is a significant economic barrier. Herein, we report the synthesis of scalable catalyst materials based on randomly alloyed palladium–silver nanoparticles. These catalysts significantly lower the overall catalyst cost and simultaneously achieve a 3.4-times increase in the catalytic activity for  $\text{NO}_2^-$  hydrogenative reduction. Density functional theory (DFT) studies reveal that alloying Pd with Ag creates more favorable surface binding sites, which is the origin of the increased catalytic activity. The catalysts are also highly selective toward the production of nitrogen gas over ammonia.

**KEYWORDS:** palladium–silver alloys, nitrite reduction, microwave synthesis, density functional theory (DFT), semimetal catalysts, water treatment



## INTRODUCTION

Nitrate ( $\text{NO}_3^-$ ) is one of the most ubiquitous contaminants found in surface and groundwaters across the globe.<sup>1</sup> In some studies, it is present in nearly 70% of groundwater samples and is detected 13 times more often than other common contaminants.<sup>2</sup> Although  $\text{NO}_3^-$  is naturally present at low levels, elevated  $\text{NO}_3^-$  concentrations are derived from anthropogenic sources (e.g., septic systems and livestock and arable farming).<sup>3–7</sup> When ingested,  $\text{NO}_3^-$  is reduced *in vivo* to nitrite ( $\text{NO}_2^-$ ), which can cause methemoglobinemia (“blue-baby syndrome”). Additionally,  $\text{NO}_2^-$  can react with amines and amides in the gastrointestinal tract to form potentially carcinogenic *N*-nitroso compounds.<sup>3,5,7,8</sup> Additionally, long-term exposure to low levels of  $\text{NO}_3^-$  has been linked to higher rates of various forms of cancer,<sup>7</sup> making  $\text{NO}_3^-$  and  $\text{NO}_2^-$  two of the most important pollutants to address in drinking water treatment. Catalytic treatment has emerged as a promising method to eliminate  $\text{NO}_3^-$  *via* hydrogenation to  $\text{N}_2$  gas or ammonia ( $\text{NH}_3$ ). In comparison to  $\text{NO}_3^-$  removal *via* ion exchange (IX) resins, catalytic hydrogenation is an attractive alternative because it produces fewer waste byproducts.<sup>9,10</sup> In contrast to biological denitrification, catalytic reactors can also be more rapidly implemented.  $\text{H}_2$  gas used in catalysis has also been shown to have a substantially lower environmental footprint than organic electron donors used in biological reactors.<sup>9–12</sup> However, the application of an economically feasible and environmentally sustainable  $\text{NO}_3^-$  catalytic treatment technology requires the identification of catalyst materials with improved activities and longevities.<sup>13,14</sup>

In 1993, Hörold and co-workers published a seminal result that demonstrated selective  $\text{NO}_3^-$  and  $\text{NO}_2^-$  removal from drinking water using a supported palladium (Pd) catalyst.<sup>15</sup> These catalysts use atomic hydrogen, Pd metal, and a promoter metal to reduce  $\text{NO}_3^-$  to  $\text{NO}_2^-$  and then to either  $\text{N}_2$  or  $\text{NH}_3$ . In recent years, catalysts based on less expensive platinum-group metals (PGMs; e.g., ruthenium, Ru) or non-noble metals (e.g.,  $\text{Ni}_2\text{P}$ ) have attracted much attention as they can directly reduce  $\text{NO}_3^-$  without a promoter metal. However, these catalysts have limited potential for drinking water treatment: Ru-based catalysts suffer competitive adsorption between  $\text{NO}_3^-$  and  $\text{NO}_2^-$ , which severely inhibits  $\text{NO}_3^-$  hydrogenation in the presence of  $\text{NO}_2^-$ .<sup>16</sup>  $\text{Ni}_2\text{P}$  catalysts require extremely low pH ranges (*ca.* 2–4) for efficient  $\text{NO}_3^-$  reduction; at pH ranges near typical drinking water (6.5–8.5 per the USEPA), they show little activity for  $\text{NO}_3^-$  conversion (*i.e.*, <25% after 24 h).<sup>17</sup> Additionally, both Ru and  $\text{Ni}_2\text{P}$  catalysts are almost completely selective ( $\geq 90\%$ ) toward  $\text{NH}_3$  as the end product, which is undesirable in drinking water treatment. Thus, Pd continues to be the catalyst of choice, though its high cost ( $\$88.54 \text{ g}^{-1}$ ; APMECH, Inc.; February 2020) inspires continued efforts to identify alternatives.

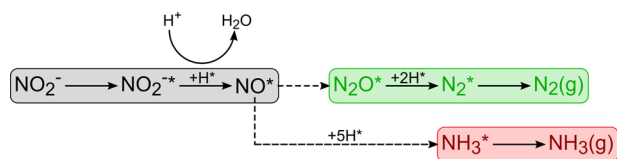
Received: April 3, 2020

Revised: June 20, 2020

Published: June 22, 2020

To achieve this aim, the mechanisms responsible for the reduction of  $\text{NO}_3^-$  and  $\text{NO}_2^-$  using  $\text{H}_2$  as the reducing agent need to be better understood. Through real-time techniques (e.g., *in situ* attenuated total reflection infrared (ATR-IR) spectroscopy)<sup>18,19</sup> and density functional theory (DFT) studies,<sup>20–22</sup> the key intermediate reactions that influence both the catalytic activity and selectivity have been identified (Scheme 1; see Figure S1 for a more detailed mechanism).<sup>21,22</sup>

### Scheme 1. Catalytic Reaction Pathways for $\text{NO}_2^-$ Hydrogenation<sup>a</sup>



<sup>a</sup>Green and red pathways represent selectivity toward  $\text{N}_2$  and  $\text{NH}_3$ , respectively, as determined from the  $\text{NO}^*$  step. The \* symbol represents adsorbed states.

Additionally, many efforts have been made to enhance catalyst design at a molecular level to achieve higher rates for  $\text{NO}_3^-$  and  $\text{NO}_2^-$  hydrogenation. Investigations into the regulation of Pd and promoter metal surface coverage,<sup>23,24</sup> the effects of PdNP morphology (i.e., exposed crystal facets),<sup>25</sup> and the role of secondary metal additives (e.g., Au and Cu)<sup>22,26,27</sup> have all proven important in optimizing catalyst activity. Further, the uses of “exotic” supports, including both carbon-based materials and ceramic metal oxides, have been shown to enhance catalyst stability and activity. Unsaturated carbon-based supports (e.g., reduced graphene or carbon nanofibers), where delocalization of  $\pi$ -electrons between the catalyst and support leads to enhanced metal reactivity, are increasingly used in a variety of catalytic and electrocatalytic applications.<sup>28,29</sup> Strong metal–support interactions (SMSI) induced by metal oxide supports can also enhance activation of adsorbate–adsorbent bonds.<sup>30</sup> For example, Vannice and co-workers demonstrated SMSI between metallic Pd islands and titania ( $\text{TiO}_2$ ) enhance the rate of carbon monoxide (CO) methanation *versus* Pd–silica (Pd– $\text{SiO}_2$ ) or Pd–alumina (Pd– $\text{Al}_2\text{O}_3$ ).<sup>31,32</sup> The benefits of  $\text{TiO}_2$ -supported catalysts over  $\text{SiO}_2$ - or  $\text{Al}_2\text{O}_3$ -supported catalysts have also been demonstrated in the aqueous hydrogenation of  $\text{NO}_3^-$  and  $\text{NO}_2^-$ .<sup>30,33</sup>

Previous studies from our group have demonstrated that binary alloys of Pd or Rh with a Group 11 metal (Cu, Ag, or Au; all of which are unable to oxidatively cleave  $\text{H}_2$  gas) provide enhanced activity over monometallic Pd or Rh catalysts in gas-phase hydrogenation reactions.<sup>34,35</sup> The observed increase in hydrogenation activity is derived through interatomic d-band mixing (electronic) and atomic ensemble (ligand) effects that weaken H-binding on the catalyst surfaces.<sup>36,37</sup> Alloying of rare and expensive metals such as Pd or Rh with more abundant metals also provides a convenient way to reduce the overall cost of catalyst production. In our work, combined experimental and theoretical results revealed that PdAu, RhAu, and RhAg alloys elevate the measured turnover frequencies (TOFs) for cyclohexene hydrogenation by 4.5–10 times compared to pure Pd or Rh.<sup>34,35</sup> More recently, we reported that the  $\text{NO}_2^-$  hydrogenation activity of alloyed PdAuNP catalysts was 2.5 times greater than pure PdNP catalysts due to beneficial ensemble effects.<sup>10</sup> However, PdAu-based catalysts do little to

address the financial concerns facing Pd-based catalytic systems. In comparison, Ag ( $\$0.60 \text{ g}^{-1}$ ; APMEEX, Inc.; February 2020 *vs*  $\$53.01 \text{ g}^{-1}$  Au; APMEEX, Inc.; February 2020) is an attractive economic alternative for the synthesis of Pd alloys.

In this work, we present a scalable synthetic method that uses microwave ( $\mu\text{wI}$ )-assisted heating for the preparation of palladium–silver nanoparticles ( $\text{Pd}_x\text{Ag}_{100-x}\text{NPs}$ ) with tunable compositions ( $x = 50\text{--}90$ ) for application in aqueous-phase  $\text{NO}_2^-$  hydrogenation.  $\mu\text{wI}$  heating has long been studied for industrial-scale reactions,<sup>38</sup> because it is highly amenable to fast reactions in continuous-flow reactors.<sup>39</sup>  $\text{NO}_2^-$  was chosen as the initial target species because it is the first intermediate product of reductive  $\text{NO}_3^-$  decomposition. The reduction of  $\text{NO}_3^-$  to  $\text{NO}_2^-$  requires a secondary promoter metal (e.g., Cu or In), which would introduce additional variables that would hinder the clear activity–structure relationship of the nanoparticle catalysts. However, the hydrogenation of the intermediate  $\text{NO}_2^-$  to  $\text{N}_2$  does not require a secondary promoter metal. Therefore,  $\text{NO}_2^-$  reduction to  $\text{N}_2$  is an ideal model reaction with which to study explicitly the structure–reactivity correlations as a function of PdAg catalyst composition. A series of  $\text{Pd}_x\text{Ag}_{100-x}\text{NPs}$  were synthesized with target Pd:Ag ratios ranging from 1:1 to 9:1; the actual compositions were confirmed using a variety of characterization techniques (i.e., inductively coupled plasma optical emission spectroscopy (ICP-OES), scanning transmission electron microscopy with two-dimensional energy-dispersive X-ray spectroscopy (STEM-2D-EDS), powder X-ray diffraction (PXRD), and X-ray photoelectron spectroscopy (XPS)). All of the  $\text{Pd}_x\text{Ag}_{100-x}\text{NP}$  catalysts studied displayed an enhanced cost-normalized activity for  $\text{NO}_2^-$  hydrogenation when compared to analogous monometallic PdNP catalysts ( $\geq 1.2$  times). Furthermore, the  $\text{Pd}_x\text{Ag}_{100-x}\text{NP}$  catalysts achieved  $>95\%$  selectivity toward  $\text{N}_2$  production *versus*  $\text{NH}_3$ . Supporting DFT studies confirm that randomly alloyed PdAgNP surfaces provide optimized binding energies for the key reaction species, resulting in faster overall  $\text{NO}_2^-$  hydrogenation in water.

## RESULTS AND DISCUSSION

**Microwave-Assisted Synthesis of  $\text{Pd}_x\text{Ag}_{100-x}\text{NPs}$  ( $x = 50\text{--}90$ ).** To the best of our knowledge, there are only a handful of reports on the synthesis of alloyed PdAg nanostructures, most of which are not practical at scale due to factors such as reagent selection (e.g., palladium(II) trifluoroacetate,  $(\text{CF}_3\text{COO})_2\text{Pd}$ ; polyallylamine hydrochloride (PAH)),<sup>40,41</sup> reaction conditions (e.g., the use of carboxylated cellulose nanocrystals or  $\gamma$ -irradiation)<sup>42,43</sup> or poor control over particle morphology (e.g., large size ranges within single samples).<sup>44</sup> Here, we demonstrate a convenient, scalable, and highly reproducible synthesis of near-monodisperse  $\text{Pd}_x\text{Ag}_{100-x}\text{NPs}$  *via* a  $\mu\text{wI}$ -assisted polyol method, which utilizes only common chemicals (i.e., nitrate salts, ethylene glycol, and water). Briefly,  $\text{Pd}(\text{NO}_3)_2$  and  $\text{AgNO}_3$  precursors were co-dissolved in water and subsequently added to a solution of poly(vinylpyrrolidone) (PVP) in ethylene glycol (EG) at  $150^\circ\text{C}$  under  $\mu\text{wI}$  (see Experimental Section and Figure S2 for preparation details). The compositions of the as-synthesized  $\text{Pd}_x\text{Ag}_{100-x}\text{NPs}$  were dictated by the molar ratio of the Pd(II) and Ag(I) precursors employed. Individual experiments with target compositions of  $x = 50, 60, 70, 80, 90$  resulted in products with actual compositions correspond-

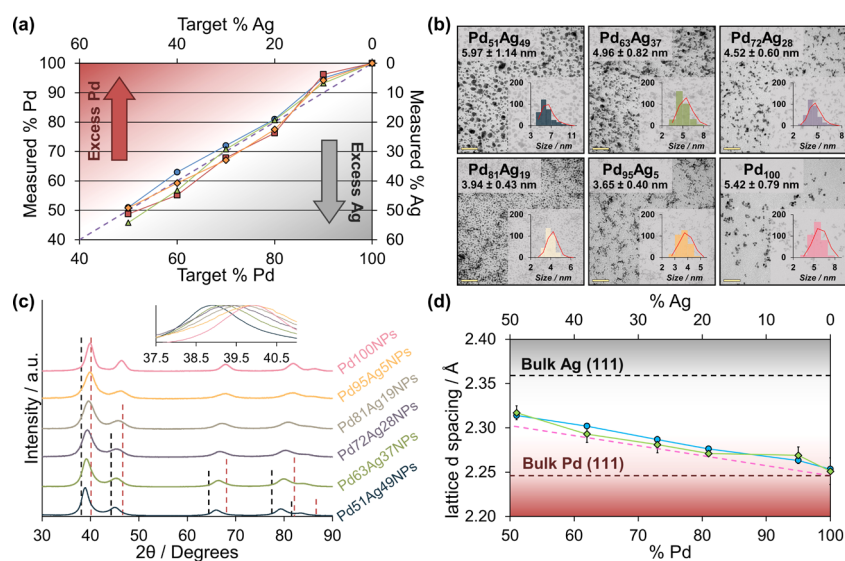


**Figure 1.** (a) Comparison of measured nanoparticle compositions by different techniques *versus* the percent target composition (dashed purple line): ICP-OES (blue circles), XPS (red squares), PXRD (green triangles), and STEM-EDS (orange diamonds). (b) Representative TEM images for each Pd<sub>x</sub>Ag<sub>100-x</sub>NP composition. The insets show size distributions, with histograms of measured sizes. Scale bars shown are 50 nm. (c) PXRD patterns for Pd<sub>x</sub>Ag<sub>100-x</sub>NPs showing peak shifting with the decrease in the Pd content. The inset shows the expansion of the (111) peak maxima. The vertical dashed lines represent expected  $2\theta$  values for reflections from FCC bulk Pd (burgundy) and FCC bulk Ag (black) at relative intensities. (d) Vegard's plot of calculated lattice d-spacings from PXRD (blue circles) and high-resolution (HR)-TEM (green diamonds) as a function of composition. The dashed horizontal lines represent reference values for bulk Pd (burgundy) and bulk Ag (black); the dashed pink line indicates the calculated lattice d-spacings for target compositions using a weighted average of Pd and Ag.

ing to  $x = 51, 63, 72, 81,$  and  $95$  (based on ICP-OES data; Figure 1a and Table S1). Low-resolution transmission electron microscopy (TEM) characterization revealed a majority of cuboctahedral particles, consistent with the equilibrium shape of face-centered cubic (FCC) nanocrystals.<sup>45,46</sup> The various compositions had sizes ranging from 3.6 to 6.0 nm, and each composition displayed high monodispersity ( $\sigma < \pm 20\%$ ) (Figure 1b). PXRD analysis confirmed random alloying in bulk NP samples (Figure 1c). According to Vegard's Law, the (111) Bragg reflections of the Pd<sub>x</sub>Ag<sub>100-x</sub>NPs are expected to appear at the compositionally weighted average of the (111) reflections for pure Pd (expected  $40.1^\circ$ ) and pure Ag (expected  $38.1^\circ$ ) as measured by ICP-OES. The experimental PXRD patterns were in close agreement, with Pd<sub>95</sub>Ag<sub>5</sub>NPs, displaying a maximum (111) reflection at  $2\theta_{\max} = 39.83^\circ$  (Pd<sub>90</sub>Ag<sub>10</sub>NP calculated at  $39.8^\circ$ ) and Pd<sub>51</sub>Ag<sub>49</sub>NPs displaying a maximum (111) reflection at  $2\theta_{\max} = 38.92^\circ$  (Pd<sub>50</sub>Ag<sub>50</sub>NP calculated at  $39.0^\circ$ ). No additional (111) shoulders were observed, indicating complete alloying of Pd and Ag, as expected due to the miscibility of Pd and Ag across a wide range of compositions.<sup>47</sup>

Random alloying was further confirmed by high-resolution transmission electron microscopy (HR-TEM) and measurement of the NP lattice spacing (Figures 2 and S3–S7). HR-TEM analysis of Pd<sub>95</sub>Ag<sub>5</sub>NPs yielded lattice d-spacing of 2.269 Å for the (111) planes, which closely agrees with the theoretical spacing of 2.252 Å (Figure 2a; pure FCC Pd (111) = 2.246 Å; pure Ag (111) = 2.359 Å). As the percentage of Pd decreased, the measured lattice d-spacing increased until Pd<sub>51</sub>Ag<sub>49</sub>NPs (2.317 Å). 2D-EDS elemental maps for the Pd and Ag atoms (Figure 2b–e) further verified random alloying of the two metals, with no evidence of segregation or core-shell segregation. Our previous studies have also found for alloyed and core@shell PdAg structures, surface Pd atoms can be stabilized by adsorbates on the surface (e.g., H<sup>48</sup> and N<sup>22</sup>).

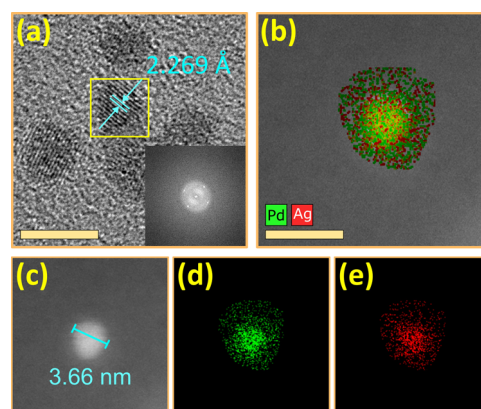


**Figure 2.** (a) HR-TEM image of unsupported Pd<sub>95</sub>Ag<sub>5</sub>NPs showing the lattice d-spacing of 2.269 Å; the inset shows the fast Fourier transform. (b) 2D-EDS overlay of Pd and Ag atomic mappings on a Pd<sub>95</sub>Ag<sub>5</sub>NP. Scale bars shown are 5 nm. (c) High-angular annular dark-field STEM (HAADF-STEM) image of a Pd<sub>95</sub>Ag<sub>5</sub>NP measured at 3.66 nm. (d) Atomic distribution of Pd in the imaged NP. (e) Atomic distribution of Ag in the imaged NP.

This hinders the surface segregation of the secondary metal, because Pd is a stronger binding metal than Ag. The stronger Pd–adsorbate bond will counteract the segregation of Ag even with low adsorbate coverage. Similar conclusions have also been drawn from calculations of IrAg<sup>49</sup> and many other Ag-based alloy systems.<sup>48</sup> The surface composition assessed by XPS also agreed with the bulk composition values as measured by ICP-OES (Figure 1a and Table S1). A slight Ag-bias was observed on the surface of the NPs by XPS due to the difference in the nobility of Pd and Ag, as evidenced by their galvanic potentials. Ag is expected to preferentially migrate to the NP surfaces in their native oxidized state, because Ag (less noble,  $E = 0.80$  V) is slightly more reactive to oxidation than

Pd ( $E = 0.92$  V).<sup>50</sup> XPS was also used to provide a glimpse of oxidation state distribution of surface atoms, which are exposed to air and thus may be oxidized to some extent (Figures S8–S13 and Table S2). Subsurface atoms, which are only coordinated with other metal atoms, were expected to be zerovalent. XPS analysis of Pd<sub>x</sub>Ag<sub>100-x</sub>NPs revealed a larger percentage of surface Pd atoms in the Pd(II) state as “x” increased, similar to the previous work on PdAuNPs.<sup>10,34</sup> Both pure PdNPs and Pd<sub>95</sub>Ag<sub>5</sub>NPs were found to have Pd(II)/Pd(0) ratios of 1:4 by XPS, while Pd<sub>51</sub>Ag<sub>49</sub>NPs showed no visible peak for Pd(II). As the total number of Pd atoms increases at the surface, it can be concluded that more atoms will become oxidized, which results in a stronger signal during XPS analysis, as has been observed for other Pd-based alloys.<sup>22,34,51</sup> Interestingly, the incorporation of Ag into the Pd lattice had no effect on the Pd 3d binding energy (Table S3), contrary to some previous studies of Pd–Ag alloy nanoparticles.<sup>52</sup> For all Ag-containing NPs, XPS analysis revealed that the Ag atoms at the particle surface were present as Ag(I) (Table S4), as expected from Ag’s preference to migrate to the particle surface where it is exposed to oxygen.

**Performance of Silica-Supported Pd<sub>x</sub>Ag<sub>100-x</sub>NP Catalysts.** The as-synthesized Pd<sub>x</sub>Ag<sub>100-x</sub>NPs were supported on synthesized amorphous silica (SiO<sub>2</sub>) *via* direct deposition (see Methods for detailed procedure). For each catalyst, a total metal loading of between 1 and 2 wt % (wt % = Pd + Ag) was targeted; the actual loadings were determined by ICP-OES (1.3–1.7 wt %; Table S5). TEM analysis of the supported catalysts confirmed no change in the NP size or morphology once supported (Figure S14 for example; average diameter for unsupported *versus* supported PdNPs was 5.42 ± 0.79 nm *vs* 5.52 ± 0.68 nm, respectively). SiO<sub>2</sub> was initially used as the support material, because it is relatively inert and should not influence the catalytic properties of the NPs.<sup>34,53,54</sup> Catalytic kinetic experiments for NO<sub>2</sub><sup>-</sup> reduction were performed in batch reactors using H<sub>2</sub> gas as the reducing agent (for details, see Methods). All catalysts displayed *pseudo*-first-order kinetics (Figure S15), from which the apparent first-order rate constants were calculated. The rate constants were then normalized to the total Pd loading of each catalyst (Figure 3, red diamonds) and used to determine TOFs based on active surface sites on the catalysts (Figure S16). TOFs were

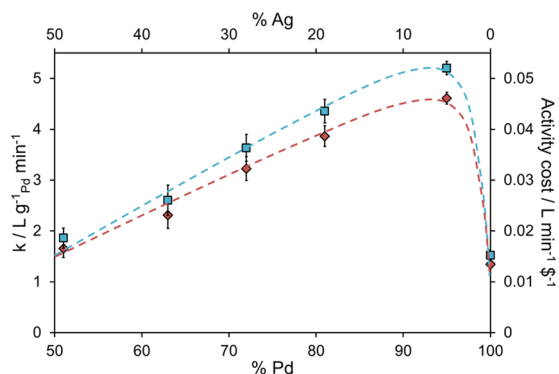


**Figure 3.** First-order rate constants (normalized to total Pd as wt % of catalyst) in units of liters per grams of Pd per min (red diamonds, red dashed line) for aqueous NO<sub>2</sub><sup>-</sup> reduction by SiO<sub>2</sub>-supported Pd<sub>x</sub>Ag<sub>100-x</sub>NP catalysts. Catalyst activity normalized to the total cost of metal (Pd + Ag) for each Pd<sub>x</sub>Ag<sub>100-x</sub>NP-SiO<sub>2</sub> catalyst (blue squares, blue dashed line).

normalized on the basis of the total number of active surface sites (assuming Pd is active for NO<sub>2</sub><sup>-</sup> hydrogenation, while Ag is not) present in each supported catalyst (calculated assuming regular cuboctahedral NP morphology, using average NP sizes measured by TEM and the weight percent Pd loadings obtained from ICP-OES).

The catalytic activity showed an increasing trend as the nanoparticle composition became more Pd-rich, with the peak activity exhibited by the Pd<sub>95</sub>Ag<sub>5</sub>NP-SiO<sub>2</sub> catalyst. The calculated activity for Pd<sub>95</sub>Ag<sub>5</sub>NP-SiO<sub>2</sub> was 4.61 L g<sub>Pd</sub><sup>-1</sup> min<sup>-1</sup> (TOF = 2.78 min<sup>-1</sup>), which is 3.4-times greater than the pure PdNP-SiO<sub>2</sub> catalyst ( $k = 1.35$  L g<sub>Pd</sub><sup>-1</sup> min<sup>-1</sup>; TOF = 1.35 min<sup>-1</sup>; *cf.*  $k = 1.3$  L g<sub>Pd</sub><sup>-1</sup> min<sup>-1</sup> from Hörold et al. and  $k = 2.0$  L g<sub>Pd</sub><sup>-1</sup> min<sup>-1</sup> from Seraj et al.).<sup>10,15</sup> However, all Pd<sub>x</sub>Ag<sub>100-x</sub>NP-SiO<sub>2</sub> catalysts displayed enhanced activities over the pure PdNP-SiO<sub>2</sub> catalyst, a trend similar to other low-cost Pd-based alloy NPs that our group has studied before.<sup>26</sup> When Cu was incorporated into PdNP-based catalysts, Pd<sub>80</sub>Cu<sub>20</sub>NPs exhibited the highest activity for NO<sub>2</sub><sup>-</sup> hydrogenation ( $k = 1.91$  L g<sub>Pd</sub><sup>-1</sup> min<sup>-1</sup>), though all alloys outperformed monometallic PdNPs. Interestingly, the Pd<sub>81</sub>Ag<sub>19</sub>NP-SiO<sub>2</sub> catalyst moderately outperforms the Pd<sub>95</sub>Ag<sub>5</sub>NP-SiO<sub>2</sub> when using TOF as a metric for activity (2.88 *vs* 2.78 min<sup>-1</sup>; Figure S16). All catalyst compositions maintained a N<sub>2</sub> selectivity of over 98% for 2 h reaction (Table S6, rows 1–6), in close agreement with previously reported selectivity values for Pd-based NO<sub>2</sub><sup>-</sup> catalysts (75–99%).<sup>14,15,55</sup> Recent studies have suggested that selectivity for N<sub>2</sub> can decrease as NO<sub>2</sub><sup>-</sup> hydrogenation approaches full conversion and the adsorbed N:H ratio decreases.<sup>19</sup> While it is possible that some of our catalysts could exhibit increased NH<sub>3</sub> selectivity if NO<sub>2</sub><sup>-</sup> hydrogenation continued longer than 2 h, this would still be a small amount of the total nitrogen conversion.

**Economic Benefit of Alloyed PdAgNPs.** As discussed earlier, it is also important to evaluate the activity per total cost of the PdAgNP-SiO<sub>2</sub> catalyst manufactured. Assuming that the costs for each catalyst are derived primarily from the metal content,<sup>14</sup> the calculated activities have been normalized to the US \$ cost for each catalyst (Figure 3, blue squares, and Table S7, column 5). The peak activity per \$ is found for the Pd<sub>95</sub>Ag<sub>5</sub>NP-SiO<sub>2</sub> catalyst (0.05205 L min<sup>-1</sup> USD<sup>-1</sup>), which shows an activity-per-cost enhancement of 3.4-times compared to an analogous PdNP-SiO<sub>2</sub> catalyst (0.01522 L min<sup>-1</sup> USD<sup>-1</sup>). In fact, all Pd<sub>x</sub>Ag<sub>100-x</sub>NP-SiO<sub>2</sub> catalysts display an improvement over the activity of pure PdNP catalysts. Despite not showing improvement when normalized to total metal (Pd + Ag; 0.85 L g<sub>metal</sub><sup>-1</sup> min<sup>-1</sup> *vs* 1.35 L g<sub>metal</sub><sup>-1</sup> min<sup>-1</sup>), when normalized to metal cost, the Pd<sub>51</sub>Ag<sub>49</sub>NP-SiO<sub>2</sub> catalyst shows a 22% increase in performance-per-cost over pure PdNP-SiO<sub>2</sub> (0.01859 L min<sup>-1</sup> USD<sup>-1</sup> *vs* 0.01522 L min<sup>-1</sup> USD<sup>-1</sup>).

**Nitrogen Binding Energy at Pd<sub>x</sub>Ag<sub>100-x</sub> Surface Ensembles.** Our previous work indicated that the N-binding energy can be an effective reaction descriptor to estimate the NO<sub>2</sub><sup>-</sup> reduction activity of a catalyst surface, thus allowing a better understanding of trends in catalytic activity.<sup>22</sup> The 3-fold triatomic ensemble on a close-packed (111) FCC surface is the smallest repeat unit that determines the site-specific activity of a catalyst.<sup>37,56</sup> Here, using DFT calculations, average N-binding energies at the four possible triatomic ensembles (Pd<sub>3</sub>, Pd<sub>2</sub>Ag<sub>1</sub>, PdAg<sub>2</sub>, and Ag<sub>3</sub>) on randomly alloyed Pd<sub>75</sub>Ag<sub>25</sub>(111) surfaces were calculated (Figure 4a). The results indicate that as the Ag ratio is increased in a triatomic ensemble, the average

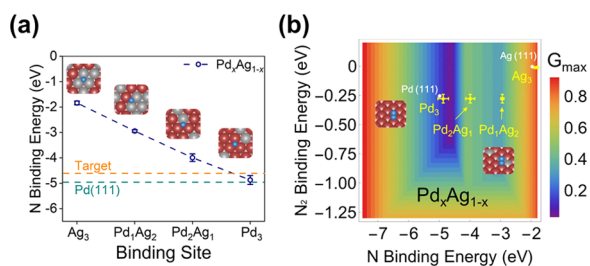


**Figure 4.** (a) Calculated N-binding energies at the four triatomic ensembles ( $\text{Ag}_3$ ,  $\text{Ag}_2\text{Pd}_1$ ,  $\text{Ag}_1\text{Pd}_2$ , and  $\text{Pd}_3$ ) on randomly alloyed  $\text{Pd}_{0.75}\text{Ag}_{0.25}(111)$  surfaces. The orange dashed line represents the optimal N-binding energy estimated from the volcano model. The green dashed line represents the N-binding energy on a Pd(111) surface. The insets show the representative adsorption geometries of N at the ensembles. (b) Nitrite reduction volcano model with the plotted Pd(111), Ag(111), and the triatomic ensembles on randomly alloyed  $\text{Pd}_{0.75}\text{Ag}_{0.25}(111)$  surfaces. The insets show the representative adsorption geometries of  $\text{N}_2$  at Pd(111) and the Pd-atop on  $\text{Pd}_{0.75}\text{Ag}_{0.25}(111)$ . Each error bar was calculated from ten sampled binding sites from ten generated randomly alloyed  $\text{Pd}_{0.75}\text{Ag}_{0.25}(111)$  surfaces. Blue, burgundy, and gray spheres represent N, Pd, and Ag, respectively.

N-binding energy becomes correspondingly weaker (*i.e.*, more positive). The adsorption geometries (Figure 4a, inset) show that N is preferentially bound at the 3-fold hollow site of the triatomic ensemble in a manner similar to the binding modes of C, O, and H on close-packed surfaces of some other bimetallic alloys.<sup>48,57,58</sup> To estimate the apparent reactivity as a function of surface binding energies, we previously derived a volcano plot for the energy of the rate-determining step of  $\text{NO}_2^-$  reduction as a function of both N- and  $\text{N}_2$ -binding energies (Figure 4b). Based on the known N- and  $\text{N}_2$ -binding energies, we can estimate the binding energies of other reaction-related adsorbates for  $\text{NO}_2^-$  hydrogenation from the linear scaling relationship found between the binding energies of N and these other adsorbates.<sup>22</sup> With this binding information, we can estimate the reaction free energy of each elementary step of the hydrogenation pathway in the reaction network.  $G_{\text{max}}$  is then defined as the rate-determining step of a specific pathway with the lowest free energy compared to other competing pathways, assuming given N- and  $\text{N}_2$ -binding energies (Figure 4b). Due to the multiple mechanistic pathways available (Scheme 1), the plot displays two peaks. The volcano plot suggests that the rate-determining steps are the direct dissociation of NO (left peak) and the activation of N–O after hydrogenation (right peak). Only reaction thermodynamics were considered in our model due to the high consistency between this volcano model and those from previous experimental studies.<sup>10,22,26</sup> More quantitative analysis of the reaction mechanism would require a more detailed kinetic analysis.<sup>59</sup> It is clear that the NO dissociation step is the most energetically favorable ( $G_{\text{max}} \leq 0.2$ ). An overlay of the four triatomic ensembles on the volcano plot reveals that Pd-rich sites (*i.e.*,  $\text{Pd}_3$ ) are closest to the peak when compared with Ag-related sites ( $\text{Pd}_2\text{Ag}_1$ ,  $\text{Pd}_1\text{Ag}_2$ ,  $\text{Ag}_3$ ) or even pure Pd(111). Thus, while pure Pd(111) ensembles are highly active for  $\text{NO}_2^-$  reduction, alloying a small amount of Ag with Pd enhances the reactivity of these Pd surfaces (*i.e.*,  $\text{Pd}_3$  in Figure 4). This is similar to previous conclusions in other Pd-based systems (*e.g.*, PdAu, PdCu, and Au@Pd): although pure Pd sites are proven to be highly active compared to inert metallic surfaces, alloying inert elements such as Ag into Pd can lead to

a significant activity enhancement over pure Pd surfaces<sup>10,22,26</sup> due to electronic and strain effects between the alloyed atoms.<sup>60,61</sup> Additionally, the results reveal that while N-binding is tunable with the ratio of Pd to Ag in a triatomic ensemble, the  $\text{N}_2$ -binding energy remains relatively constant because  $\text{N}_2$  is always adsorbed at Pd-atop sites (Figure 4b, inset), which are independent of the precise triatomic ensemble composition. Overall, the results from our DFT calculations found that alloying Ag with Pd weakens N-binding in triatomic ensembles compared to pure Pd(111) and hence creates more favorable conditions (lower  $G_{\text{max}}$ ) for the reduction of  $\text{NO}_2^-$ . These theoretical results are in excellent agreement with our experimental observations (Figure 3).

#### Effect of the Support Material on $\text{NO}_2^-$ Reduction.

Three  $\text{Pd}_x\text{Ag}_{100-x}\text{NP}$  compositions (PdNPs,  $\text{Pd}_{90}\text{Ag}_{10}\text{NPs}$ , and  $\text{Pd}_{70}\text{Ag}_{30}\text{NPs}$ ) were supported on various redox-active supports (*i.e.*, where the metal oxide contains defects caused by reduced metal species) to better understand the potential synergistic benefits of supporting the randomly alloyed nanoparticles on electronically active support materials. The supports studied were  $\gamma$  alumina ( $\gamma\text{-Al}_2\text{O}_3$ ; amphoteric; SA =  $78 \text{ m}^2 \text{ g}^{-1}$ ), Aeroxide P25 titania ( $\text{TiO}_2$ ; reducible; SA =  $63 \text{ m}^2 \text{ g}^{-1}$ ), and amorphous cobalt oxide ( $\text{Co}_3\text{O}_4$ ; reducible; SA =  $66 \text{ m}^2 \text{ g}^{-1}$ ) (see Figure S17 for  $\text{N}_2$  sorption isotherms). The as-synthesized nanoparticles were characterized *via* ICP-OES (Table S8), LR-TEM (Figures S18 and S19), PXRD (Figure S20), HR-TEM (Figures S21–S23), and XPS (Figures S24–S26 and Table S9) to confirm consistency in particle morphology and composition across each synthesis. These characterizations reveal that the developed  $\mu\text{WI}$ -assisted polyol synthesis method produces similarly sized particles that incorporate similar amounts of Pd and Ag every time. ICP-OES analysis revealed catalyst loadings between 1.1 and 2.3 wt % (total metal; Table S10). Catalysis experiments were conducted in batch reactors to assess the effect of catalyst support on  $\text{NO}_2^-$  hydrogenation by  $\text{Pd}_x\text{Ag}_{100-x}\text{NP}$  catalysts. All catalysts displayed *pseudo*-first-order reaction kinetics as per the previously studied  $\text{SiO}_2$ -supported PdAgNPs (Figure S27), from which apparent first-order rate constants were calculated; the rate constants were normalized to TOF (Figure 5a and Table S11).

The trends in measured activities of catalysts supported on different materials were found to be similar to those of  $\text{SiO}_2$ -supported catalysts. When normalized to the Pd-mass loading,

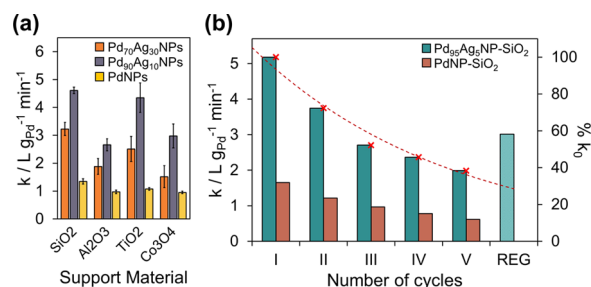


**Figure 5.** (a) Activities in units of liters per g Pd per min for  $\text{NO}_2^-$  reduction over  $\text{Pd}_{70}\text{Ag}_{30}\text{NPs}$ ,  $\text{Pd}_{90}\text{Ag}_{10}\text{NPs}$ , and PdNPs supported on  $\text{SiO}_2$ ,  $\gamma\text{-Al}_2\text{O}_3$ ,  $\text{TiO}_2$ , and  $\text{Co}_3\text{O}_4$ . (b) Comparison of catalytic activity loss between  $\text{Pd}_{95}\text{Ag}_5\text{NP-SiO}_2$  and PdNP- $\text{SiO}_2$  over multiple cycles of  $\text{NO}_2^-$  hydrogenation. The striped “REG” bar shows the regeneration of  $\text{Pd}_{95}\text{Ag}_5\text{NP-SiO}_2$  by  $\text{H}_2$  gas at  $60^\circ\text{C}$ . The red “X”s and red dashed line demonstrate the exponential loss of activity ( $R^2 = 0.966$ ).

the peak activity for each support was observed for the nominal Pd<sub>90</sub>Ag<sub>10</sub>NPs, followed closely by the Pd<sub>70</sub>Ag<sub>30</sub>NPs. In each family, the Pd<sub>70</sub>Ag<sub>30</sub>NPs displayed an activity enhancement ranging from 60 to 135% over the PdNPs. The Pd<sub>90</sub>Ag<sub>10</sub>NPs gave activity increases between 175 and 300% over pure PdNPs. This trend is similar to that of the SiO<sub>2</sub>-supported catalysts. When the activities are normalized to the costs of the total metal used for each nanoparticle catalyst, the enhancements in the activity-cost show an identical trend (Table S11). Interestingly, the SiO<sub>2</sub>-supported catalysts outperform the catalysts using other supports, regardless of NP composition. This could be due to different support morphologies (e.g., amorphous vs crystalline, surface area differences, etc.) resulting in different surface coverages and available surface sites, as evidenced by experimentally derived TOFs (Figure S28). Further studies are needed to derive the effects of the support materials for NO<sub>2</sub><sup>-</sup> hydrogenation over Pd<sub>x</sub>Ag<sub>100-x</sub>NPs. The selectivity for N<sub>2</sub> gas was also unaffected by supporting Pd<sub>x</sub>Ag<sub>100-x</sub>NPs on more electronically active supports. For each catalyst, the selectivity to N<sub>2</sub> over NH<sub>3</sub> was greater than 95% (Table S6, rows 7–15, and Figure S29).

**Environmental Relevancy.** The use of Pd catalysts for widespread potable water treatment is also hindered by concerns over natural supply limits, as Pd is an expensive noble metal. However, previous work has revealed that a full-scale IX system uses ca. 3.6 lbs. of salt for every 1000 gallons of water that is treated.<sup>62</sup> Additionally, we recently showed that a small (0.5 million gallons per day) treatment plant would spend at least \$433 000 for salt alone to remove NO<sub>3</sub><sup>-</sup> via IX to treat one billion gallons of water.<sup>14</sup> However, the corresponding cost for Pd to remove this nitrate would be \$55 000, only 13% of the cost of IX salt, assuming that batch reactor rates could be achieved and the catalysts last for this treatment period.<sup>63</sup> Previous life cycle analyses from our group have also indicated that a drinking water treatment plant processing 2.5 million gallons per day would only require 7.8 kg of Pd every 10 years.<sup>13</sup> (For reference, US consumption in 2017 was 89 000 kg Pd.<sup>64</sup>) The implementation of a precious metal-based catalyst system for a worldwide process such as water treatment is strongly reliant on ensuring high activity throughout the catalyst's lifetime. To investigate the longevity of the PdAgNP-based catalysts, Pd<sub>95</sub>Ag<sub>5</sub>NP-SiO<sub>2</sub> (i.e., the optimal catalyst in terms of both alloy composition and support) was subjected to repeated NO<sub>2</sub><sup>-</sup> reduction cycles in batch systems. We also analyzed the activity of a PdNP-SiO<sub>2</sub> catalyst over repeated reactions as a control comparison (see Methods for details). The total Pd normalized rate constants were calculated and compared for each cycle (Figure 5b). Initially, the activities of each catalyst closely agreed with those measured in single-run batch reactor experiments (5.18 and 1.65 L g<sub>Pd</sub><sup>-1</sup> min<sup>-1</sup>, for Pd<sub>95</sub>Ag<sub>5</sub>NP-SiO<sub>2</sub> and PdNP-SiO<sub>2</sub>, respectively). The activity was found to decrease by ca. 15–25% upon each consecutive cycle in an exponential manner ( $\frac{k}{k_0} = 118.44 e^{-0.237 \cdot \text{cycle}}$ ). Interestingly, both catalysts displayed similar patterns of activity loss with each repeated cycle (Table S12). After five cycles, the Pd<sub>95</sub>Ag<sub>5</sub>NP-SiO<sub>2</sub> catalyst maintained 43% of its original activity, as compared to 37% for the pure PdNP-SiO<sub>2</sub> catalyst. Also, despite a nearly 60% loss of activity, the Pd<sub>95</sub>Ag<sub>5</sub>NP-SiO<sub>2</sub> catalyst still displayed higher activity than pristine PdNP-SiO<sub>2</sub> catalysts. After completing multiple NO<sub>2</sub><sup>-</sup> reduction cycles, the nanoparticle catalysts were characterized to analyze possible deactivation

mechanisms. Comparison of pre-recycled catalysts and post-recycled catalysts revealed no major change in the particle morphology or catalyst composition (TEM, Figures S30 and S31; PXRD, Figure S32; and XPS, Figures S33 and S34; Tables S13 and S14). From this complementary characterization, it is clear that measurable physical changes (e.g., dealloying, particle agglomeration, and metal dissolution) are not responsible for the observed loss of catalyst activity. Previous results from packed-bed reactor systems operated continuously for 23 days also indicate that activity eventually reaches steady state;<sup>14</sup> our results demonstrate that reactivating a used catalyst restores its activity (Figure 5b; teal striped bar).

Herein, we have developed a convenient and scalable μWI-assisted method for the synthesis of near-monodisperse, alloyed Pd<sub>x</sub>Ag<sub>100-x</sub>NPs, which leverages the use of common reagents (i.e., metal nitrate salts, ethylene glycol, and water). This methodology allows for the reproducible control over the ratio of Pd:Ag (i.e., the value of *x*). The synthesis also preserves the particle morphology (e.g., shape, size) between different batches. These PdAgNP catalysts provide significant activity-cost improvements over analogous monometallic Pd-based catalysts based on lower total metal costs and concomitantly achieving faster reaction rates. Alloying Pd with Ag (\$88.54 vs \$0.60 g<sup>-1</sup>, respectively; APMEX, Inc.; February 2020) drastically lowers the total metal costs for the manufacture of NP-based catalysts. Further, our experimental and theoretical results show that PdAgNP catalysts exploit electronic effects intrinsic to these nanoalloys, which creates N-binding surface sites that are energetically more favorable than those on monometallic PdNPs. In turn, this engenders faster reaction rates and correspondingly higher catalyst activity. The utility of PdAgNP catalysts has been exemplified here in the aqueous-phase hydrogenation of NO<sub>2</sub><sup>-</sup>, which is a relevant model reaction for NO<sub>3</sub><sup>-</sup> treatment in potable water. The PdAgNP catalysts discovered in this work also hold potential for applications in a number of other industrial settings, including the destruction of other oxyanion water contaminants and in hydrogenation chemistry.

## EXPERIMENTAL SECTION

**Materials.** Materials were used as received with no further purification or treatment, unless otherwise noted. K<sub>2</sub>PdCl<sub>4</sub> (99%; Acros Organics), Pd(NO<sub>3</sub>)<sub>2</sub>·nH<sub>2</sub>O (99.9%; Strem Chemicals), AgNO<sub>3</sub> (99.9%; Alfa Aesar), poly(vinylpyrrolidone) (PVP; {C<sub>6</sub>H<sub>9</sub>NO}<sub>*n*</sub>; ⟨M<sub>w</sub>⟩ = 58000; Alfa Aesar), NaBH<sub>4</sub> (98%; Alfa Aesar), and ethylene glycol (EG; 99.8%; Fisher Scientific) were used for all nanoparticle synthesis reactions. Pluronic P-123, poly(ethylene glycol) (⟨M<sub>w</sub>⟩ = 5800; Sigma-Aldrich), HCl (12.1 M; Fisher Scientific), NaOH (98%; Sigma-Aldrich), *n*-decane (99%; Acros Organics), NH<sub>4</sub>F (96%; Alfa Aesar), tetraethyl orthosilicate (TEOS; Si(OC<sub>2</sub>H<sub>5</sub>)<sub>4</sub>; 98%; Alfa Aesar), and Co(NO<sub>3</sub>)<sub>2</sub>·6H<sub>2</sub>O (99%; Sigma-Aldrich) were used to synthesize the amorphous silica (SiO<sub>2</sub>) and cobalt oxide (Co<sub>3</sub>O<sub>4</sub>) supports. γ-phase alumina (γ-Al<sub>2</sub>O<sub>3</sub>; 3 μm APS powder; 99.97%; Alfa Aesar) and Aeroxide P25 (TiO<sub>2</sub>; Acros Organics) were purchased and used post-acid washing for nanoparticle supports. NaNO<sub>2</sub> (99%; Sigma-Aldrich) was used as the nitrite source for kinetic experiments; KH<sub>2</sub>PO<sub>4</sub> (99%; Sigma-Aldrich) and K<sub>2</sub>HPO<sub>4</sub> (98%; Sigma-Aldrich) were used as pH control for kinetic reactions; and H<sub>2</sub> gas (99.99%; Praxair) was used as the reducing agent for kinetic experiments. All reagents and solvents were analytical grades unless otherwise stated.

**Analytical Methods.** Powder X-ray diffraction (PXRD) measurements were performed using an R-Axis Spider diffractometer (Rigaku Corporation) equipped with a Cu  $K\alpha$  source ( $\lambda = 1.5418 \text{ \AA}$ ) operated at 40 kV and 40 mA. The scan speed was  $10^\circ \text{ min}^{-1}$ , with a sampling width of  $0.01^\circ$ . Transmission electron microscopy (TEM) samples were prepared by dispersing nanoparticles in ethanol and drop casting the dispersion onto 200 mesh copper Formvar grids (Ted Pella, Inc.) before air drying the sample. Nanoparticle size was analyzed by manually measuring particles using the imaging software Image-J (<https://imagej.nih.gov/ij/>); for each sample, a minimum of 300 measurements was taken to calculate a mean particle diameter and corresponding standard deviation. Low-resolution TEM (LR-TEM) images were obtained using an FEI Tecnai transmission electron microscope operated at 80kV. High-resolution TEM (HR-TEM) images and energy-dispersive X-ray spectroscopy (EDS) spectra were obtained using a JEOL 2010F transmission electron microscope equipped with an Oxford EDS detector and operated at 200 keV with a 0.19 nm point to point resolution. Lattice spacing was measured from HR-TEM images using the image processing software DigitalMicrograph (Gatan Inc.). X-ray photoelectron spectroscopy (XPS) samples were prepared by drop casting the nanoparticles dispersed in ethanol onto glass slides and letting the solvent evaporate. The analysis was performed on a KRATOS X-ray Photoelectron Spectrometer-Axis Ultra DLD; the XPS spectra were recorded using a monochromated Al  $K\alpha$  X-ray source ( $h\nu = 1486.5 \text{ eV}$ ), hybrid optics (employing a magnetic and electrostatic lens simultaneously), and a multichannel plate coupled to a hemispherical photoelectron kinetic analyzer. All spectra were obtained *via* four sweeps for signal averaging, a dwell time of 1800 ms, an aperture slot of  $300 \times 700 \mu\text{m}^2$ , a pass energy of 20 eV, and a step of 0.1 eV. Due to sample charging and to minimize consequential band shape distortion, the spectra were recorded with the KRATOS charge neutralizer (20 eV electrons) with the sample not grounded. The recorded XPS spectra were analyzed using CasaXPS software to deconvolute peaks and to determine sample composition by peak area integration using KRATOS sensitivity factors for each element.

Percent metal loading and bulk elemental analysis of catalysts were determined by inductively coupled plasma optical emission spectroscopy (ICP-OES) on a Varian 710-ES (Agilent Technologies, Inc.) using the ICP Expert II Software (Agilent Technologies, Inc.). The samples were prepared for ICP-OES by digesting 5 mg of each catalyst in concentrated nitric acid ( $\text{HNO}_3$ ; 6  $\text{cm}^3$ ; trace metal grade) heated to 100  $^\circ\text{C}$ . Samples were diluted to 25  $\text{cm}^3$  with deionized water and left overnight to allow any undigested support material to settle; 11  $\text{cm}^3$  of each sample was then collected for analysis. Nitrite concentrations were determined by ion chromatography (IC) using a Dionex ICS-2100 equipped with a Dionex IonPac AS18 column and a Dionex EGC II KOH EluGen Cartridge (run under the program-controlled concentration with a flow of  $1 \text{ cm}^3 \text{ min}^{-1}$ ). Ammonia concentrations were measured *via* Hach colorimetric kits using the salicylate method ( $0.2\text{--}2.5 \text{ mg L}^{-1} \text{ NH}_3\text{-N}$ ). The measurement of pH was performed with a FiveEasy Plus Benchtop pH-Conductivity Meter (Mettler Toledo). The surface area of the support materials was measured by  $\text{N}_2$  physisorption at 77 K using a Quantachrome Autosorb-1 system. The samples

were first evacuated at 200  $^\circ\text{C}$  before beginning adsorption studies.

**Nanoparticle Synthesis.** All nanoparticles were synthesized by the polyol reduction method using microwave-assisted heating,  $\mu\text{wI}$ , as described in previous publications.<sup>35,65,66</sup> All  $\mu\text{wI}$  reactions were carried out in a MARS 5 microwave reactor with a maximum power of 1600 W (2.45 GHz) (CEM Corp.). The reactions were carried out with a fiber-optic temperature feedback control (RTP300+ temperature sensor; CEM Corp.) and magnetic stirring (450 rpm), while open to air. The reaction flask consisted of a 50  $\text{cm}^3$  round-bottom flask fitted with a water-cooled reflux condenser.

For monometallic PdNPs, excess PVP (222 mg; 20 equiv of monomers per mmol of Pd) was dissolved in ethylene glycol (EG; 15  $\text{cm}^3$ ) and the solution was heated over 6 min to 150  $^\circ\text{C}$  with  $\mu\text{wI}$  under stirring. Separately,  $\text{K}_2\text{PdCl}_4$  (32.6 mg; 0.10 mmol) was dissolved in EG (5  $\text{cm}^3$ ) with sonication. The  $\text{Pd}^{\text{II}}$ /EG solution was then directly added to the hot PVP/EG solution *via* disposable poly(tetrafluoroethylene) (PTFE) tubing (i.d. 1.0 mm) by a programmable syringe pump (WPI, Inc.) at a rate of  $300 \text{ cm}^3 \text{ h}^{-1}$ . After complete addition (1 min), the reaction was held at constant temperature and stirred for 30 min. After complete reaction, the reaction flask was transferred to an ice-water bath to quench the reaction. The resulting NPs were then isolated with the addition of acetone (ca. 70  $\text{cm}^3$ ) and centrifugation (5500 rpm; 5 min). The supernatant was then discarded, and the NPs were redispersed in ethanol (ca. 10  $\text{cm}^3$ ) with sonication to remove excess PVP. The NPs were then isolated again by precipitation with hexanes (ca. 80  $\text{cm}^3$ ) and centrifugation (5500 rpm; 5 min). The supernatant was discarded, and the NPs were left to air dry overnight before being stored in 50 mL polypropylene tubes as a glassy film.

$\text{Pd}_x\text{Ag}_{100-x}$ NPs, with “ $x$ ” representing the molar percent of Pd present in the alloy, were synthesized in a novel manner, by adapting methods from previous work using  $\mu\text{wI}$  heating.<sup>10,34</sup> The synthesis matrix was initially optimized to determine the ideal conditions. Generally, excess PVP (55.5 mg; 5 molar equiv of monomers per mmol of total metal, *i.e.*, Pd + Ag) was dissolved in EG (15  $\text{cm}^3$ ) and heated with  $\mu\text{wI}$  to 150  $^\circ\text{C}$  over 6 min. Separately, the metal precursors,  $\text{Pd}(\text{NO}_3)_2 \cdot n\text{H}_2\text{O}$  and  $\text{AgNO}_3$ , were dissolved in deionized water (5  $\text{cm}^3$ ) with sonication and added to the PVP/EG solution *via* PTFE tubing and a syringe pump at an addition rate of  $300 \text{ cm}^3 \text{ h}^{-1}$ . The molar amounts of each precursor used were based on the nominal target ratio of the NPs, maintaining the total molar amount of metal at 0.10 mmol. After 30 min, the reaction was quenched in an ice-water bath, and the NPs were isolated following the same procedure as above.

**Support Preparation.** Amorphous  $\text{SiO}_2$  was prepared using the previously published methods.<sup>67</sup> Pluronic P-123 (2.4 g) was completely dissolved in an HCl solution (86 g; 1.03 M) with stirring (450 rpm) at 40  $^\circ\text{C}$  (solution became clear).  $n$ -Decane (30  $\text{cm}^3$ ; 0.154 mol) was added as the swelling agent, and the solution was stirred (1000 rpm) for at least 2 h to ensure homogeneity.  $\text{NH}_4\text{F}$  (0.028 g; 0.76 mmol) was added, immediately followed by the dropwise addition of TEOS (5.6  $\text{cm}^3$ ; 25.1 mmol). Stirring at 40  $^\circ\text{C}$  continued for 20 h resulting in an opaque slurry. This slurry was transferred to a square polyethylene bottle and placed into a static convection oven at 100  $^\circ\text{C}$  for 48 h. After cooling, the slurry was then filtered, and the isolated solid was repeatedly washed with distilled water to remove excess surfactant and then calcined at 550  $^\circ\text{C}$  for 6 h in

a box furnace. The surface area (SA) as measured by N<sub>2</sub> physisorption was 502 m<sup>2</sup> g<sup>-1</sup>.

Amorphous Co<sub>3</sub>O<sub>4</sub> was synthesized by adapting a previously reported method.<sup>68</sup> Pluronic P-123 (4.86 g) was completely dissolved in a 1:1 ethanol/water solution of NaOH (120 cm<sup>3</sup>; 0.50 M) *via* magnetic stirring in a closed glass vessel. NH<sub>4</sub>F (0.056 g; 1.52 mmol) was added to the reaction flask. The pH of the solution was then lowered to 13.1 by the dropwise addition of aqueous HCl (1.07 M). The solution was stirred for 20 min, before *n*-decane (30 cm<sup>3</sup>; 154 mmol) was added dropwise as the swelling agent, and the solution was stirred for another 30 min to ensure homogeneity. A solution of Co(NO<sub>3</sub>)<sub>2</sub>·6H<sub>2</sub>O (1.64 g; 5.64 mmol) in ethanol (12.0 cm<sup>3</sup>) was then added; upon addition, the Co<sup>II</sup> turned from red to blue as it complexed with Cl<sup>-</sup> ions. After approximately 15 min of stirring at room temperature, the solution turned from blue to green. After 2 h, the solution turned to black with the formation of Co<sub>3</sub>O<sub>4</sub>. The mixture was then stirred at 35 °C for 20 h before being transferred to a square 250 cm<sup>3</sup> Nalgene bottle sealed with PTFE tape and placed in a conventional oven at 82 °C for 48 h. The resulting slurry was then isolated *via* centrifugation (7000 rpm; 5 min), washed repeatedly with ethanol until the supernatant was clear, and then calcined in a box furnace open to air at 400 °C for 5 h (heat ramping of 1.0 °C min<sup>-1</sup>). The SA as measured by N<sub>2</sub> physisorption was 66 m<sup>2</sup> g<sup>-1</sup>.

Commercially purchased  $\gamma$  alumina ( $\gamma$ -Al<sub>2</sub>O<sub>3</sub>; SA = 78 m<sup>2</sup> g<sup>-1</sup>) and titania (TiO<sub>2</sub>; SA = 63 m<sup>2</sup> g<sup>-1</sup>) were first washed with acid before being used as nanoparticle supports. Generally, the support material (2.0 g) was dispersed in deionized water (20 cm<sup>3</sup>) *via* sonication and rapid stirring (800 rpm) in a 20 cm<sup>3</sup> glass scintillation vial with a micromagnetic stir bar. Concentrated nitric acid (HNO<sub>3</sub>) was added dropwise *via* a pipette to achieve a final concentration of 0.5 M. The mixture was then stirred at 85 °C for 1 h. The acid-washed support material was isolated by vacuum filtration, washed with copious amounts of deionized water and ethanol, and dried in a 60 °C oven overnight.

**Nanoparticle Loading on Supports.** Catalysts were prepared by direct deposition of synthesized nanoparticles onto support materials to achieve approximately 1.5 wt % total metal loading. Briefly, the support material (*a*-SiO<sub>2</sub>,  $\gamma$ -Al<sub>2</sub>O<sub>3</sub>, P25 TiO<sub>2</sub>, or *a*-Co<sub>3</sub>O<sub>4</sub>; 250 mg) was suspended in distilled water (10 cm<sup>3</sup>) by sonication and rapid stirring (1200 rpm) in a 20 cm<sup>3</sup> glass scintillation vial with a micromagnetic stir bar. Separately, PVP-capped Pd<sub>x</sub>Ag<sub>100-x</sub>NPs or PdNPs (approximately 5.3 mg) were dispersed in ethanol (10 cm<sup>3</sup>) *via* sonication. NP suspensions were then added dropwise to the support suspension. The resulting mixtures were then stirred for 10 min (800 rpm) and sonicated for 10 min. This process was repeated for at least three cycles. The resulting slurry was then filtered *via* vacuum, resulting in a clear supernatant. The isolated catalysts were washed extensively with water and ethanol and then dried overnight in a 60 °C oven.

**Kinetic Experiments and Modeling.** Nitrite reduction experiments were performed in batch-scale reactors (60 cm<sup>3</sup> glass vials sealed with a rubber septum) at ambient temperature (23 ± 1 °C) and atmospheric pressure with magnetic stirring. Phosphate buffer (0.1 M; 40 cm<sup>3</sup>; pH 6.4) and supported NP catalyst (0.5 g L<sup>-1</sup>) were added to the reaction vessel. The suspension was sparged by bubbling H<sub>2</sub> gas through the system at a rate of 0.120 L min<sup>-1</sup> for a minimum of 1 h; this ensured both the medium and headspace

of the reactor were completely saturated with H<sub>2</sub>. The reduction reaction was then initiated by spiking with a 100  $\mu$ L aliquot of NaNO<sub>2</sub> (0.87 M; 40 000 ppm as NO<sub>2</sub><sup>-</sup>) to give an initial concentration of 100 mg L<sup>-1</sup> NO<sub>2</sub><sup>-</sup> in the reaction flask. The samples were taken at regular time intervals for a total reaction time of 2 h for N-species analysis. The total volume of the sample removed was  $\leq$ 10% of the total solution volume. It was also assumed that the catalyst concentration in the reactor remained constant throughout the experiment as the suspension was continuously stirred to ensure homogeneity in the system. All NO<sub>2</sub><sup>-</sup> reactions were conducted in triplicate to derive rate constants for each unique catalyst composition and support pairing. To test catalyst longevity, a series of five consecutive NO<sub>2</sub><sup>-</sup> reduction reactions were performed. Initially, phosphate buffer (60 cm<sup>3</sup>) and the catalyst were sparged with H<sub>2</sub> gas for 1 h, and an initial reaction was performed. At the end of each reaction, the reaction flask was resparged with H<sub>2</sub> gas for 1 h, before being respiked with a new aliquot of NO<sub>2</sub><sup>-</sup> to bring the initial concentration back to 100 mg L<sup>-1</sup>. Again, catalyst concentration was assumed constant as samples were removed from a well-mixed homogeneous mixture. Catalyst regeneration was performed by flowing H<sub>2</sub> gas over the used, dried catalyst at 250 cm<sup>3</sup> min<sup>-1</sup> at 60 °C for 4 h. Nitrite reduction was found to obey *pseudo*-first-order kinetics for the consumption of  $\geq$ 80% of initial NO<sub>2</sub><sup>-</sup>. Initial first-order rate constants were normalized to the total wt % of Pd for each catalyst tested. The rate constants were obtained from the linear regression of the natural log of NO<sub>2</sub><sup>-</sup> concentration *versus* time plots, using eq 1

$$-\frac{dC_{\text{NO}_2^-}}{dt} \left( \frac{1}{C_{\text{Pd}}} \right) = k_{\text{obs}} C_{\text{NO}_2^-} \quad (1)$$

where  $C_{\text{NO}_2^-}$  is the concentration of aqueous nitrite (mg NO<sub>2</sub><sup>-</sup> L<sup>-1</sup>),  $C_{\text{Pd}}$  is the concentration of the metal in the catalyst (g<sub>Pd</sub> L<sup>-1</sup>), and  $k_{\text{obs}}$  is the observed first-order rate constant normalized by Pd catalyst concentration (L g<sub>Pd</sub><sup>-1</sup> min<sup>-1</sup>). Turnover frequencies (TOFs) were calculated from the product of the measured *pseudo*-first-order rate constants and the initial number of nitrite ions divided by the number of active surface sites as calculated from an idealized cuboctahedral nanoparticle, following eq 2

$$\text{TOF} = \frac{k' \times N_{0,\text{NO}_2^-}}{\text{ss}_{\text{Pd}}} \quad (2)$$

where  $k'$  is the first-order rate constant,  $N_{0,\text{NO}_2^-}$  is the number of initial NO<sub>2</sub><sup>-</sup> ions, and  $\text{ss}_{\text{Pd}}$  is the number of available Pd surface sites on the catalyst. The number of Pd surface sites on each catalyst was calculated assuming regular cuboctahedral NP morphology, using average NP sizes measured by TEM and the Pd weight percent loadings obtained *via* ICP-OES (see Supporting Information page 23, for a complete walkthrough of calculation). Catalyst selectivity was measured under the assumption that aqueous NO<sub>2</sub><sup>-</sup> reduction goes to one of two final end products, N<sub>2</sub> or NH<sub>3</sub>.<sup>4,15,69</sup> The selectivity was calculated by comparing the concentration of NH<sub>3</sub>, as mg<sub>N</sub> L<sup>-1</sup>, after complete reaction (2 h) to the total amount of NO<sub>2</sub><sup>-</sup>, as mg<sub>N</sub> L<sup>-1</sup>, lost throughout the reaction, using eq 3.

$$\text{selectivity (\%)} = 100 - \frac{[\text{NH}_3]_{\text{produced}}}{[\text{NO}_2^-]_{\text{lost}}} \quad (3)$$

External mass-transfer limitations were assessed by calculating the Damkohler coefficient, which is a comparative ratio of the reaction rate to the rate of mass transfer, defined as

$$Da = \frac{k_{\text{obs}} \times d_p}{k_L} \quad (4)$$

where  $k_{\text{obs}}$  is the observed pseudo-first-order reaction rate,  $d_p$  is the diameter of the support particles, and  $k_L$  is the rate of mass transfer. The parameter  $k_L$  was obtained from the Sherwood number correlation, defined as

$$Sh = \frac{k_L \times d_p}{D_{\text{app}}} \quad (5)$$

assuming that the lower limit for the Sherwood number is 2 as particles become smaller than a micron.<sup>70</sup> For the fastest observed reaction rate, this value was  $Da = 1.40 \times 10^{-5}$ , which is much less than 1, indicating that external mass-transfer limitations are negligible (see [Supporting Information](#), p. 24 for details). Intraparticle mass-transfer limitations were assessed using the Weisz–Prater,  $C_{\text{WP}}$ ,<sup>71,72</sup> defined as

$$C_{\text{WP}} = \frac{R^2 \times k_{\text{obs}} \times \tau}{D \times \theta} \quad (6)$$

where  $R$  is the radius of the supported catalyst [ $m$ ],  $k_{\text{obs}}$  is the pseudo-first-order rate constant [ $\text{min}^{-1}$ ],  $\tau$  is the tortuosity of the catalyst [ $-$ ],  $D$  is the diffusion coefficient of  $\text{NO}_2^-$  in bulk water [ $\text{m}^2 \text{sec}^{-1}$ ], and  $\theta$  is the porosity [ $-$ ]. For the fastest observed rate constant, the Weisz–Prater parameter was calculated to be  $C_{\text{WP}} = 4.81 \times 10^{-5}$ , which is much less than 1, indicating that intraparticle mass-transfer limitations are negligible (see [Supporting Information](#), p. 24 for details).

**Computational Methods.** All density functional theory (DFT) calculations were performed using the VASP code,<sup>73</sup> with the generalized gradient approximation, Perdew–Burke–Ernzerhof functional, and projector augmented wave methods.<sup>74,75</sup> Kohn–Sham wave functions were expanded in a plane wave basis with the energy cutoff set as 400 eV.<sup>76</sup> A ( $3 \times 3 \times 1$ )  $k$ -point mesh was used to sample the Brillouin zone using the method by Monkhorst and Pack.<sup>77</sup> Spin polarization was applied for the calculation of the N-species in vacuum. Convergence was defined when all of the forces in the atomistic system became lower than 0.05 eV  $\text{\AA}^{-1}$ .

All of the catalytic surfaces were modeled as four-layer, ( $3 \times 3$ ), (111) slabs, with at least 12  $\text{\AA}$  of vacuum at the  $z$ -direction to separate images. The bottom two layers were fixed in bulk positions, while the top two layers were unconstrained. The use of lattice constants of each slab was based on Vegard's law according to the composition of the alloying elements.<sup>57,78</sup> Ten randomly alloyed  $\text{Pd}_{75}\text{Ag}_{25}$ (111) surfaces were generated using our Python code based on the Atomic Simulation Environment library.<sup>79</sup> Since our  $\mu\text{WI}$ -assisted synthesis process was kinetically controlled,<sup>80,81</sup> the binding site sampling from a sufficient amount of randomly generated surfaces was found to be more representative than the calculations on ordered alloy structures.<sup>82</sup> Each average N or  $\text{N}_2$  binding energy was sampled from ten binding sites on these surfaces. The binding energies of N or  $\text{N}_2$  ( $E_{\text{b}}$ ) were calculated using eq 7

$$E_{\text{b}} = E_{\text{tot}} - E_{\text{slab}} - E_{\text{ads}} \quad (7)$$

where  $E_{\text{tot}}$  is the total energy of the adsorption system,  $E_{\text{slab}}$  is the total energy of the bare slab, and  $E_{\text{ads}}$  is the total energy of the adsorbate in vacuum.

## ■ ASSOCIATED CONTENT

### Supporting Information

The Supporting Information is available free of charge at <https://pubs.acs.org/doi/10.1021/acscatal.0c01538>.

PXRD, TEM, XPS, HR-TEM, and EDS data for the synthesized nanoparticles and catalysts, additional experimental and computational details (PDF)

## ■ AUTHOR INFORMATION

### Corresponding Authors

**Graeme Henkelman** – Department of Chemistry, The University of Texas at Austin, Austin, Texas 78712, United States; [orcid.org/0000-0002-0336-7153](https://orcid.org/0000-0002-0336-7153); Phone: +1 512 471 4106; Email: [henkelman@utexas.edu](mailto:henkelman@utexas.edu)

**Simon M. Humphrey** – Department of Chemistry, The University of Texas at Austin, Austin, Texas 78712, United States; [orcid.org/0000-0001-5379-4623](https://orcid.org/0000-0001-5379-4623); Phone: +1 512 471 0312; Email: [smh@cm.utexas.edu](mailto:smh@cm.utexas.edu)

**Charles J. Werth** – Department of Civil, Architectural, and Environmental Engineering, The University of Texas at Austin, Austin, Texas 78712, United States; [orcid.org/0000-0002-8492-5523](https://orcid.org/0000-0002-8492-5523); Phone: +1 512 232 1626; Email: [werth@utexas.edu](mailto:werth@utexas.edu)

### Authors

**Jacob P. Troutman** – Department of Civil, Architectural, and Environmental Engineering and Department of Chemistry, The University of Texas at Austin, Austin, Texas 78712, United States

**Hao Li** – Department of Chemistry, The University of Texas at Austin, Austin, Texas 78712, United States

**Alison M. Haddix** – Department of Civil, Architectural, and Environmental Engineering, The University of Texas at Austin, Austin, Texas 78712, United States

**Benjamin A. Kienle** – Department of Civil, Architectural, and Environmental Engineering, The University of Texas at Austin, Austin, Texas 78712, United States

Complete contact information is available at: <https://pubs.acs.org/10.1021/acscatal.0c01538>

### Notes

The authors declare no competing financial interest.

## ■ ACKNOWLEDGMENTS

The authors thank Dr. Pranaw Kunal (formerly UT Austin) for his guidance in nanoparticle synthesis. The authors also thank Dr. R. Eric Sikma (UT Austin; physisorption), Dr. Dwight Romanovicz (UT Austin; LR-TEM), Michelle Mikesch (UT Austin; LR-TEM), Dr. Hugo Celio (UT Austin; XPS), Dr. Karalee Jarvis (UT Austin; HR-TEM, STEM-EDS), and Dr. Vincent Lynch (UT Austin; PXRD) for assistance with particle characterization. Funding for this work was provided by the National Science Foundation under Grant Nos. CBET-1922504 and CHE-1807847 and the Welch Foundation (F-1738, SMH & F-1841, GH). Computational resources were provided by the Texas Advanced Computing Center and the XSEDE program.

## ■ REFERENCES

(1) Liu, A.; Ming, J.; Ankumah, R. O. Nitrate contamination in private wells in rural Alabama, United States. *Sci. Total Environ.* **2005**, *346*, 112–120.

- (2) Nolan, B. T.; Stoner, J. D. Nutrients in groundwaters of the conterminous United States, 1992-1995. *Environ. Sci. Technol.* **2000**, *34*, 1156–1165.
- (3) Fewtrell, L. Drinking-water nitrate, methemoglobinemia, and global burden of disease: A discussion. *Environ. Health Perspect.* **2004**, *112*, 1371–1374.
- (4) Yin, Y. B.; Guo, S.; Heck, K. N.; Clark, C. A.; Coonrod, C. L.; Wong, M. S. Treating water by degrading oxyanions using metallic nanostructures. *ACS Sustainable Chem. Eng.* **2018**, *6*, 11160–11175.
- (5) Townsend, A. R.; Howarth, R. W.; Bazzaz, F. A.; Booth, M. S.; Cleveland, C. C.; Collinge, S. K.; Dobson, A. P.; Epstein, P. R.; Holland, E. A.; Keeney, D. R.; Mallin, M. A.; Rogers, C. A.; Wayne, P.; Wolfe, A. H. Human health effects of a changing nitrogen cycle. *Front. Ecol. Environ.* **2003**, *1*, 240–246.
- (6) Seiler, R. L. Combined use of  $^{15}\text{N}$  and  $^{18}\text{O}$  of nitrate and  $^{11}\text{B}$  to evaluate nitrate contamination in groundwater. *Appl. Geochem.* **2005**, *20*, 1626–1636.
- (7) Weyer, P. J.; Cerhan, J. R.; Kross, B. C.; Hallberg, G. R.; Kantamneni, J.; Breuer, G.; Jones, M. P.; Zheng, W.; Lynch, C. F. Municipal drinking water nitrate level and cancer risk in older women: The Iowa women's health study. *Epidemiology* **2001**, *12*, 327–338.
- (8) Adelana, S. M. A. Nitrate health effects. *Water Encyclopedia* **2005**, *4*, 30–42.
- (9) Kapoor, A.; Viraraghavan, T. Nitrate removal from drinking water - Review. *J. Environ. Eng.* **1997**, *123*, 371–380.
- (10) Seraj, S.; Kunal, P.; Li, H.; Henkelman, G.; Humphrey, S. M.; Werth, C. J. PdAu alloy nanoparticle catalysts: Effective candidates for nitrite reduction in water. *ACS Catal.* **2017**, *7*, 3268–3276.
- (11) Lehman, S. G.; Badruzzaman, M.; Adham, S.; Roberts, D. J.; Clifford, D. A. Perchlorate and nitrate treatment by ion exchange integrated with biological brine treatment. *Water Res.* **2008**, *42*, 969–976.
- (12) Ziv-El, M. C.; Rittmann, B. E. Systematic evaluation of nitrate and perchlorate bioreduction kinetics in groundwater using a hydrogen-based membrane biofilm reactor. *Water Res.* **2009**, *43*, 173–181.
- (13) Choe, J. K.; Bergquist, A. M.; Jeong, S.; Guest, J. S.; Werth, C. J.; Strathmann, T. J. Performance and life cycle environmental benefits of recycling spent ion exchange brines by catalytic treatment of nitrate. *Water Res.* **2015**, *80*, 267–280.
- (14) Bergquist, A. M.; Choe, J. K.; Strathmann, T. J.; Werth, C. J. Evaluation of a hybrid ion exchange-catalyst treatment technology for nitrate removal from drinking water. *Water Res.* **2016**, *96*, 177–187.
- (15) Hörold, S.; Vorlop, K.-D.; Tacke, T.; Sell, M. Development of catalysts for a selective nitrate and nitrite removal from drinking water. *Catal. Today* **1993**, *17*, 21–30.
- (16) Huo, X.; Van Hoomissen, D. J.; Liu, J.; Vyas, S.; Strathmann, T. J. Hydrogenation of aqueous nitrate and nitrite with ruthenium catalysts. *Appl. Catal., B* **2017**, *211*, 188–198.
- (17) Wei, L.; Liu, D.-J.; Rosales, B. A.; Evans, J. W.; Vela, J. Mild and Selective Hydrogenation of Nitrate to Ammonia in the Absence of Noble Metals. *ACS Catal.* **2020**, *10*, 3618–3628.
- (18) Ebbesen, S. D.; Mojet, B. L.; Lefferts, L. *In situ* ATR-IR study of nitrite hydrogenation over Pd/Al<sub>2</sub>O<sub>3</sub>. *J. Catal.* **2008**, *256*, 15–23.
- (19) Zhao, Y.; Koteswara Rao, N.; Lefferts, L. Adsorbed species on Pd catalyst during nitrite hydrogenation approaching complete conversion. *J. Catal.* **2016**, *337*, 102–110.
- (20) Shin, H.; Jung, S.; Bae, S.; Lee, W.; Kim, H. Nitrite reduction mechanism on a Pd surface. *Environ. Sci. Technol.* **2014**, *48*, 12768–12774.
- (21) Guo, S.; Heck, K.; Kasiraju, S.; Qian, H.; Zhao, Z.; Grabow, L. C.; Miller, T.; Wong, M. S. Insights into nitrate reduction over indium-decorated palladium nanoparticle catalysts. *ACS Catal.* **2018**, *8*, 503–515.
- (22) Li, H.; Guo, S.; Shin, K.; Wong, M. S.; Henkelman, G. Design of a Pd-Au nitrite reduction catalyst by identifying and optimizing active ensembles. *ACS Catal.* **2019**, *9*, 7957–7966.
- (23) Garron, A.; Lázár, K.; Epron, F. Characterization by Mössbauer spectroscopy of trimetallic Pd-Sn-Au/Al<sub>2</sub>O<sub>3</sub> and Pd-Sn-Au/SiO<sub>2</sub> catalysts for denitration of drinking water. *Appl. Catal., B* **2006**, *65*, 240–248.
- (24) Marchesini, F. A.; Irusta, S.; Querini, C.; Miró, E. Nitrate hydrogenation over Pt<sub>2</sub>In/Al<sub>2</sub>O<sub>3</sub> and Pt<sub>2</sub>In/SiO<sub>2</sub>. Effect of aqueous media and catalyst surface properties upon the catalytic activity. *Catal. Commun.* **2008**, *9*, 1021–1026.
- (25) Shuai, D.; Mccalman, D. C.; Choe, J. K.; Shapley, J. R.; et al. Structure sensitivity study of waterborne contaminant hydrogenation using shape- and size-controlled Pd nanoparticles. *ACS Catal.* **2013**, *3*, 453–463.
- (26) Guy, K. A.; Xu, H.; Yang, J. C.; Werth, C. J.; Shapley, J. R. Catalytic nitrate and nitrite reduction with Pd-Cu/PVP colloids in water: Composition, structure, and reactivity correlations. *J. Phys. Chem. C* **2009**, *113*, 8177–8185.
- (27) Qian, H.; Zhao, Z.; Velazquez, J. C.; Pretzer, L. A.; Heck, N.; Wong, M. S. Supporting palladium metal on gold nanoparticles improves its catalysis for nitrite reduction. *Nanoscale* **2014**, *6*, 358–364.
- (28) Shuai, D.; Choe, J. K.; Shapley, J. R.; Werth, C. J. Enhanced activity and selectivity of carbon nanofiber supported Pd catalysts for nitrite reduction. *Environ. Sci. Technol.* **2012**, *46*, 2847–2855.
- (29) Bhat, S. A.; Rashid, N.; Rather, M. A.; Pandit, S. A.; Rather, G. M.; Ingole, P. P.; Bhat, M. A. PdAg bimetallic nanoalloy-decorated graphene: A nanohybrid with unprecedented electrocatalytic, catalytic, and sensing activities. *ACS Appl. Mater. Interfaces* **2018**, *10*, 16376–16389.
- (30) Sá, J.; Berger, T.; Föttinger, K.; Riss, A.; Anderson, J. A.; Vinek, H. Can TiO<sub>2</sub> promote the reduction of nitrates in water? *J. Catal.* **2005**, *234*, 282–291.
- (31) Vannice, M. A.; Wang, S. Y.; Moon, S. H. The effect of SMSI (strong metal-support interaction) behavior on CO adsorption and hydrogenation on Pd catalysts I. IR spectra of adsorbed CO prior to and during reaction conditions. *J. Catal.* **1981**, *71*, 152–166.
- (32) Wang, S. Y.; Moon, S. H.; Vannice, M. A. The effect of SMSI (strong metal-support interaction) behavior on CO adsorption and hydrogenation on Pd catalysts II. Kinetic behavior in the methanation reaction. *J. Catal.* **1981**, *71*, 167–174.
- (33) Wada, K.; Hirata, T.; Hosokawa, S.; Iwamoto, S.; Inoue, M. Effect of supports on Pd–Cu bimetallic catalysts for nitrate and nitrite reduction in water. *Catal. Today* **2012**, *185*, 81–87.
- (34) Kunal, P.; Li, H.; Dewing, B. L.; Zhang, L.; Jarvis, K.; Henkelman, G.; Humphrey, S. M. Microwave-assisted synthesis of Pd<sub>x</sub>Au<sub>100-x</sub> alloy nanoparticles: A combined experimental and theoretical assessment of synthetic and compositional effects upon catalytic reactivity. *ACS Catal.* **2016**, *6*, 4882–4893.
- (35) García, S.; Zhang, L.; Piburn, G. W.; Henkelman, G.; Humphrey, S. M. Microwave synthesis of classically immiscible rhodium-silver and rhodium-gold alloy nanoparticles: Highly active hydrogenation catalysts. *ACS Nano* **2014**, *8*, 11512–11521.
- (36) Sinfelt, J. H. Catalysis by alloys and bimetallic clusters. *Acc. Chem. Res.* **1977**, *10*, 15–20.
- (37) Liu, P.; Nørskov, J. K. Ligand and ensemble effects in adsorption on alloy surfaces. *Phys. Chem. Chem. Phys.* **2001**, *3*, 3814–3818.
- (38) Metaxas, A. C.; Meredith, R. J. *Industrial Microwave Heating*; Johns, A. T.; Ratcliff, G.; Platts, J. R., Eds.; Peter Peregrinus Ltd.: London, United Kingdom, 1983; p 1.
- (39) Kunal, P.; Roberts, E. J.; Riche, C. T.; Jarvis, K.; Malmstadt, N.; Brutchey, R. L.; Humphrey, S. M. Continuous Flow Synthesis of Rh and RhAg Alloy Nanoparticle Catalysts Enables Scalable Production and Improved Morphological Control. *Chem. Mater.* **2017**, *29*, 4341–4350.
- (40) Song, P.; Feng, J. J.; Guo, F. Y.; Wang, A. J. Simple polyol synthesis of porous coral-like palladium-silver alloy nanostructures with enhanced electrocatalytic activity for glycerol oxidation reaction. *J. Mater. Chem. A* **2015**, *3*, 15920–15926.
- (41) Fu, G. T.; Liu, C.; Zhang, Q.; Chen, Y.; Tang, Y. W. Polyhedral palladium-silver alloy nanocrystals as highly active and stable

- electrocatalysts for the formic acid oxidation reaction. *Sci. Rep.* **2015**, *5*, No. 13703.
- (42) Liu, H.; Wang, D.; Shang, S.; Song, Z. Synthesis and characterization of Ag-Pd alloy nanoparticles/carboxylated cellulose nanocrystals nanocomposites. *Carbohydr. Polym.* **2011**, *83*, 38–43.
- (43) Choi, S. H.; Lee, S.; Kim, S. J.; Sohn, S. H.; Kang, H. D.; Zhang, Y. P.; Lee, K. P.; Chun, J. H. Preparation of polymer-stabilized palladium-silver bimetallic nanoparticles by  $\gamma$ -irradiation and their catalytic properties for hydrogenation of cis,cis-1,3-cyclooctadiene. *Catal. Lett.* **2005**, *105*, 59–65.
- (44) Chowdhury, S. R.; Ghosh, S.; Bhattacharya, S. K. Improved catalysis of green-synthesized Pd-Ag alloy-nanoparticles for anodic oxidation of methanol in alkali. *Electrochim. Acta* **2017**, *225*, 310–321.
- (45) Frenken, J. W. M.; Stoltze, P. Are vicinal metal surfaces stable. *Phys. Rev. Lett.* **1999**, *82*, 3500–3503.
- (46) Ringe, E.; Duyne, R. P. V.; Marks, L. D. Wulff construction for alloy nanoparticles. *Nano Lett.* **2011**, *11*, 3399–3403.
- (47) Karakaya, I.; Thompson, W. T. The Ag-Pd (Silver-Palladium) System. *Bull. Alloy Phase Diagrams* **1988**, *9*, 237–243.
- (48) Li, H.; Chai, W.; Henkelman, G. Selectivity for ethanol partial oxidation: The unique chemistry of single-atom alloy catalysts on Au, Ag, and Cu(111). *J. Mater. Chem. A* **2019**, *7*, 23868–23877.
- (49) Guo, H.; Li, H.; Jarvis, K.; Wan, H.; Kunal, P.; Dunning, S. G.; Liu, Y.; Henkelman, G.; Humphrey, S. M. Microwave-Assisted Synthesis of Classically Immiscible Ag-Ir Alloy Nanoparticle Catalysts. *ACS Catal.* **2018**, *8*, 11386–11397.
- (50) Harris, D. C. *Quantitative Chemical Analysis*, 7th ed.; W. H. Freeman and Company: New York, NY, 2007; pp AP22–AP25.
- (51) Bradley, J. S.; Via, G. H.; Bonneviot, L.; Hill, E. W. Infrared and EXAFS study of compositional effects in nanoscale colloidal palladium-copper alloys. *Chem. Mater.* **1996**, *8*, 1895–1903.
- (52) Mori, K.; Sano, T.; Kobayashi, H.; Yamashita, H. Surface Engineering of a Supported PdAg Catalyst for Hydrogenation of CO<sub>2</sub> to Formic Acid: Elucidating the Active Pd Atoms in Alloy Nanoparticles. *J. Am. Chem. Soc.* **2018**, *140*, 8902–8909.
- (53) Vander Wal, R. L.; Tichich, T. M.; Curtis, V. E. Substrate-support interactions in metal-catalyzed carbon nanofiber growth. *Carbon* **2001**, *39*, 2277–2289.
- (54) Strayer, M. E.; Binz, J. M.; Tanase, M.; Kamali Shahri, S. M.; Sharma, R.; Rioux, R. M.; Mallouk, T. E. Interfacial bonding stabilizes rhodium and rhodium oxide nanoparticles on layered Nb oxide and Ta oxide supports. *J. Am. Chem. Soc.* **2014**, *136*, 5687–5696.
- (55) Prüsse, U.; Vorlop, K. D. Supported bimetallic palladium catalysts for water-phase nitrate reduction. *J. Mol. Catal. A: Chem.* **2001**, *173*, 313–328.
- (56) Li, H.; Evans, E. J.; Mullins, C. B.; Henkelman, G. Ethanol decomposition on Pd-Au alloy catalysts. *J. Phys. Chem. C* **2018**, *122*, 22024–22032.
- (57) Li, H.; Shin, K.; Henkelman, G. Effects of ensembles, ligand, and strain on adsorbate binding to alloy surfaces. *J. Chem. Phys.* **2018**, *149*, No. 174705.
- (58) Li, H.; Luo, L.; Kunal, P.; Bonifacio, C. S.; Duan, Z.; Yang, J. C.; Humphrey, S. M.; Crooks, R. M.; Henkelman, G. Oxygen reduction reaction on classically immiscible bimetallics: A case study of RhAu. *J. Phys. Chem. C* **2018**, *122*, 2712–2716.
- (59) Xu, P.; Agarwal, S.; Lefferts, L. Mechanism of nitrite hydrogenation over Pd/ $\gamma$ -Al<sub>2</sub>O<sub>3</sub> according to a rigorous kinetic study. *J. Catal.* **2020**, *383*, 124–134.
- (60) Mavrikakis, M.; Hammer, B.; Nørskov, J. K. Effect of strain on the reactivity of metal surfaces. *Phys. Rev. Lett.* **1998**, *81*, 2819–2822.
- (61) Tang, W.; Henkelman, G. Charge redistribution in core-shell nanoparticles to promote oxygen reduction. *J. Chem. Phys.* **2009**, *130*, No. 194504.
- (62) Wang, L.; Chen, A. S. C.; Wang, A.; Condit, W. E. Arsenic and Nitrate Removal from Drinking Water by Ion Exchange U. S. EPA Demonstration Project at Vale, OR Final Performance Evaluation Report, 2011, pp 1–93.
- (63) Bergquist, A. M.; Bertoch, M.; Gildert, G.; Strathmann, T. J.; Werth, C. J. Catalytic Denitrification in a Trickle Bed Reactor: Ion Exchange Waste Brine Treatment. *J. - Am. Water Works Assoc.* **2017**, *109*, E129–E151.
- (64) Singerling, S. A. *Minerals Yearbook Platinum-Group Metals*; 2017, 57.
- (65) Dahal, N.; García, S.; Zhou, J.; Humphrey, S. M. Beneficial effects of microwave-assisted heating versus conventional heating in noble metal nanoparticle synthesis. *ACS Nano* **2012**, *6*, 9433–9446.
- (66) García, S.; Anderson, R. M.; Celio, H.; Dahal, N.; Dolocan, A.; Zhou, J.; Humphrey, S. M. Microwave synthesis of Au-Rh core-shell nanoparticles and implications of the shell thickness in hydrogenation catalysis. *Chem. Commun.* **2013**, *49*, 4241–4243.
- (67) Zhang, H.; Sun, J.; Ma, D.; Bao, X.; Klein-Hoffmann, A.; Weinberg, G.; Su, D.; Schlögl, R. Unusual mesoporous SBA-15 with parallel channels running along the short axis. *J. Am. Chem. Soc.* **2004**, *126*, 7440–7441.
- (68) Dahal, N.; Ibarra, I. A.; Humphrey, S. M. High surface area mesoporous Co<sub>3</sub>O<sub>4</sub> from a direct soft template route. *J. Mater. Chem.* **2012**, *22*, 12675–12681.
- (69) Zhang, R.; Shuai, D.; Guy, K. A.; Shapley, J. R.; Strathmann, T. J.; Werth, C. J. Elucidation of nitrate reduction mechanisms on a Pd-In bimetallic catalyst using isotope labeled nitrogen species. *ChemCatChem* **2013**, *5*, 313–321.
- (70) Asai, S.; Konishi, Y.; Sasaki, Y. Mass Transfer Between Fine Particles and Liquids in Agitated Vessels. *J. Chem. Eng. Jpn.* **1988**, *21*, 107–112.
- (71) Weisz, P. B.; Prater, C. D. Interpretation of Measurements in Experimental Catalysis. *Adv. Catal.* **1954**, *6*, 143–196.
- (72) Fogler, H. S. *Elements of Chemical Reaction Engineering*, 4th ed.; Prentice Hall PTR: Upper Saddle River, NJ, 2006; p 1080.
- (73) Kresse, G.; Furthmüller, J. Efficient iterative schemes for *ab initio* total-energy calculations using a plane-wave basis set. *Phys. Rev. B* **1996**, *54*, 11169–11186.
- (74) Perdew, J. P.; Burke, K.; Ernzerhof, M. Generalized gradient approximation made simple. *Phys. Rev. Lett.* **1996**, *77*, 3865–3868.
- (75) Blöchl, P. E. Projector augmented-wave method. *Phys. Rev. B* **1994**, *50*, 17953–17979.
- (76) Kohn, W.; Sham, L. J. Self-consistent equations including exchange and correlation effects. *Phys. Rev.* **1965**, *140*, A1133–A1138.
- (77) Monkhorst, H. J.; Pack, J. D. Special points for Brillouin-zone integrations. *Phys. Rev. B* **1976**, *13*, 5188–5192.
- (78) Denton, A. R.; Ashcroft, N. W. Vegard's law. *Phys. Rev. A* **1991**, *43*, 3161–3164.
- (79) Hjorth Larsen, A.; Jørgen Mortensen, J.; Blomqvist, J.; Castell, I. E.; Christensen, R.; Dulak, M.; Friis, J.; Groves, M. N.; Hammer, B.; Hargus, C.; Hermes, E. D.; Jennings, P. C.; Bjerre Jensen, P.; Kermode, J.; Kitchin, J. R.; Leonhard Kolsbjerg, E.; Kubal, J.; Kaasbjerg, K.; Lysgaard, S.; Bergmann Maronsson, J.; Maxson, T.; Olsen, T.; Pastewka, L.; Peterson, A.; Rostgaard, C.; Schiøtz, J.; Schütt, O.; Strange, M.; Thygesen, K. S.; Vegge, T.; Vilhelmsen, L.; Walter, M.; Zeng, Z.; Jacobsen, K. W.; et al. The atomic simulation environment-A Python library for working with atoms. *J. Phys.: Condens. Matter* **2017**, *29*, 273002–273031.
- (80) Guo, H.; Fang, Z.; Li, H.; Fernandez, D.; Henkelman, G.; Humphrey, S. M.; Yu, G. Rational Design of Rhodium-Iridium Alloy Nanoparticles as Highly Active Catalysts for Acidic Oxygen Evolution. *ACS Nano* **2019**, *13*, 13225–13234.
- (81) Guo, H.; Li, H.; Fernandez, D.; Willis, S.; Jarvis, K.; Henkelman, G.; Humphrey, S. M. Stabilizer-Free CuIr Alloy Nanoparticle Catalysts†. *Chem. Mater.* **2019**, *31*, 10225–10235.
- (82) Guo, H.; Trindell, J. A.; Li, H.; Fernandez, D.; Humphrey, S. M.; Henkelman, G.; Crooks, R. M. Testing the predictive power of theory for Pd<sub>x</sub>Ir<sub>(100-x)</sub> alloy nanoparticles for the oxygen reduction reaction. *J. Mater. Chem. A* **2020**, *8*, 8421–8429.